PAPER

Check for updates

The effect of graphitized carbon on the adsorption and photocatalytic degradation of methylene blue over TiO₂/C composites

Jinlu Cai, Shenghua Hu,* Junhuai Xiang, [ID] * Honghua Zhang and Dandan Men

The TiO$_2$/C composites with approximately 40 wt% of carbon were prepared by calcination of precursors, formed from a one-pot liquid phase reaction between Ti(SO$_4$)$_2$ and flour. All TiO$_2$/C composites displayed mesoporous structures with high BET surface areas (117–138 m^2 g^{-1}) and small crystal sizes of TiO$_2$ (8–27 nm). The contents of graphitic carbon and rutile TiO$_2$ increased, while the surface area and TiO$_2$ crystal size decreased for the TiO$_2$/C composite on increasing the calcination temperature from 650 to 800 °C; when calcined at 800 °C, the anatase TiO$_2$ completely changed into rutile TiO$_2$ in the TiO$_2$/C composite. The TiO$_2$/C composite calcined at higher temperatures exhibited better adsorptive and photocatalytic degradation performance in the removal of methylene blue (MB). For the entire rutile TiO$_2$/C-800 composite, the adsorption process of MB can be well described by the pseudo-second-order kinetic model and is governed by chemical adsorption with the maximum adsorption capacity value equal to about 15 mg g^{-1}. Under continuous illumination with a 254 nm UV lamp (15 W) for 3 h, the percentage of MB (14 mg l^{-1}) photocatalytic degradation on 50 mg of TiO$_2$/C-800 was 25.1% higher than that of the maximum adsorption removal. These results suggest that the graphitized carbon has a significant effect on the adsorptivity and photocatalytic activity of the TiO$_2$/C composite.

1. Introduction

Dyes are critical materials in many industries such as textile, leather, paper, foods, pharmaceuticals, ceramics, paint, and pigment.[1–4] A lot of dyes become major water contaminants because they are discarded into watercourses as waste liquid in these industrial processes. Most dyes possess some elements or functional groups (such as metals or aromatics) that are highly toxic, mutagenic and even carcinogenic to aquatic life and human beings. Moreover, they are chemically inert and have little biodegradability under natural conditions. Therefore, it is essential to treat dye waste liquids to ensure their safe discharge into watercourses.

Dye contaminants from aqueous solutions can be treated by many methods, which fall into three categories, namely, physical, chemical and biological. The advantages and shortcomings of these methods are compared and summarized by Yagub *et al.*[1] Among them, adsorption is considered as a globally acclaimed method due to its simple process and low cost. However, the conventional adsorbents are limited by low adsorption capacity and kinetics, high regeneration cost, and column fouling. Photocatalytic oxidation is widely studied as

the most promising method.[3,4] Some photocatalysts also exhibit high adsorption capacity for the removal of dyes. Within 25 min, the percentage of MB removal from a 120 mg l^{-1} aqueous solution was 99.47% for the Fe$_3$O$_4$/activated montmorillonite (Fe$_3$O$_4$/Mt) nanocomposite (0.5 g) at 293 K.[5] The maximum adsorption amounts of malachite green, acid fuchsin and Congo red are 2963, 3307 and 1554 mg g^{-1} for ZnO nanoparticles, respectively.[6] Therefore, for organic pollutants, the integration of adsorption and photocatalytic degradation has attracted the interest of researchers and is considered a promising method.[3,7]

TiO$_2$ is widely investigated as a photocatalyst in the degradation of organic pollutants due to its strong oxidation, nontoxicity and good chemical stability.[8–14] However, pure TiO$_2$ has some drawbacks for its efficient degradation. TiO$_2$ has no affinity for hydrophobic organics due to its surface polarity.[15] It is often a tedious process to separate powdered TiO$_2$ with small particle size from liquids.[16] TiO$_2$ nanoparticles are prone to aggregation and have high photogenerated electron–hole pair recombination, leading to their lower efficiency and activity.[17,18] Thus, the combination of some adsorbents and TiO$_2$ nanoparticles has attracted much attention for enhancing photocatalytic activity in the degradation of organic contaminants.[19–25]

TiO$_2$ composites obtained by adding a co-adsorbent, doping, or depositing on other material are helpful for solving these problems. Supporting the TiO$_2$ nanoparticles on adsorbents such as activated carbon,[19] clay minerals[21,22] and calcium

Jiangxi Key Laboratory of Surface Engineering, School of Materials and Mechanical & Electrical Engineering, Jiangxi Science and Technology Normal University, Xuefu Road 589, Nanchang 330038, China. E-mail: shenghuahu@jxstnu.edu.cn; xiangjunhuai@163.com

silicate[23] is not only beneficial for improving the efficiency of photocatalysis, but also favors the separation and recovery of these catalysts from aqueous solution. These adsorbents usually have some excellent physicochemical properties such as high surface area, porous structure, large adsorption capacity, fast adsorption kinetics, good chemical and thermal stability, and low cost.[21,25] TiO_2 coupling with g-C_3N_4,[24] hybridizing with graphene-like carbon[26] or depositing on graphene[25,27] can promote the separation of photogenerated charge carriers (electrons and holes).

As promoters or supports of catalysts, carbon-based materials exhibit excellent synergistic effects due to their structural characteristics. For example, compared with pure titania, TiO_2 nanoparticles supported on active carbon,[28] graphitized carbon,[29] and carbon nanotubes[30] have higher photocatalytic performance in the degradation of dyes. The TiO_2–C composites can usually be prepared by different methods such as dip coating,[31] impregnation,[32] solvothermal/hydrothermal,[33–36] sol–gel,[28,37,38] chemical vapor deposition,[39,40] templating agent[41] and precipitation.[42] Usually, it is difficult to obtain the TiO_2–C composites containing highly dispersive TiO_2 with high concentrations due to the direct carbon adsorbents as initial materials in most of these methods. This problem can be resolved when TiO_2 and carbon are simultaneously formed by a one-step method.

In this work, TiO_2/C composites with approximately 40 wt% carbon were prepared by the calcination of precursors, formed from a one-pot liquid phase reaction between $Ti(SO_4)_2$ and flour. The obtained TiO_2/C composites displayed typical mesopores and had high surface areas. The anatase and rutile formed at high calcination temperatures are highly dispersed in the TiO_2/C composites. To evaluate their adsorption capacities and photocatalytic performance, MB was used as a probe molecule. The synergistic effects of adsorption-enrichment and photocatalytic degradation were correlated with surface properties such as pore structure, crystal phase-type and size, and graphitized carbon.

2. Experimental

2.1 Preparation of TiO_2/C composites

The TiO_2/C composites with approximately 40 wt% of carbon were prepared by combining the method of calcination with a one-pot liquid phase reaction. Specifically, 20 g of flour was slowly added to 40 ml $Ti(SO_4)_2$ aqueous solution (50 wt%) in a 250 ml beaker, and mixed well under stirring. The mixture was heated to 85 °C in a water bath and allowed to react at this temperature for about 3 h at a 130 rpm stirring rate. The obtained pasty mass (precursor) was dried for 2 h in an electrically heated drying oven at 130 °C and then transferred into a tube furnace filled with several small corundum boats. The precursor was heated at the flow rate of 5 °C min^{-1} to the desired temperature, and treated at that temperature for 2 h, with a nitrogen flow rate of 60 ml min^{-1}. The obtained solid product was filtered and washed thoroughly with boiling deionized water until no $SO_4{}^{2-}$ was detected in the filtrate. Finally, the product was dried in an oven at 120 °C for 12 h and denoted as

TiO_2/C-x, where x represents the numerical value of the calcination temperature. Pure TiO_2 was obtained by heating the corresponding composite in air at the desired temperature and was similarly denoted as TiO_2-y, where y represents the numerical value of the calcination temperature.

2.2 Characterization of TiO_2/C composites

The TiO_2 and carbon contents in the TiO_2/C composite were determined by combustion in air at 850 °C, since all carbon can be oxidized into carbon oxides.

Powder X-ray diffraction (XRD) patterns were collected on an XRD-6000 Shimadzu X-ray diffractometer using Ni-filtered Cu K$_\alpha$ radiation (Cu K$_\alpha$, $\lambda = 0.15406$ nm) equipped with a graphite monochromator. The employed voltage and current were 40 kV and 30 mA, respectively. The diffractograms were recorded in the 2θ range of 10–80° at a speed of 4° min^{-1}.

Nitrogen adsorption/desorption isotherms were measured at -196 °C on a Quantachrome Autosorb-iQ$_2$ auto-sorption analyzer. All TiO_2/C composites were outgassed in a high vacuum at 180 °C for 6 h prior to the measurements. The specific surface areas were calculated using the Brunauer–Emmett–Teller (BET) method. The pore size distributions were obtained from the desorption branch of the nitrogen adsorption/desorption isotherms by the Barrett–Joyner–Halenda (BJH) method. The micropore/mesopore volume was obtained according to the DFT (density functional theory) method.

The morphology and microstructure of the TiO_2/C composites were characterized by a field emission scanning electron microscope with an acceleration voltage of 20 kV (FE-SEM, Carl Zeiss Supra 55VP). TEM images of samples were observed on a high-resolution transmission electron microscope at an accelerating voltage of 200 kV (TEM, JEM-2100).

Photocurrent-time curves were measured on an Electrochemical Workstation (660E, Shanghai Chenhua Instruments Co. Ltd., China) using a conventional three-electrode quartz cell system with 0.5 mol l^{-1} Na_2SO_4 electrolyte solution. In this system, the platinum electrode, saturated calomel electrode and TiO_2/C composite/ITO glass electrode were used as the counter electrode, reference electrode and working electrode, respectively. The same 15 W UV lamp as in the photocatalytic degradation of MB was used as the light source in the photoelectrochemical experiment and was about 6 cm away from the working electrode. The procedure for fabricating the TiO_2/C composite/ITO glass electrode was as follows: first, the suspension of the appropriate TiO_2/C composite powder was dispersed in 10 ml of anhydrous ethanol and ultrasonicated for 1 h. The suspension was slowly dropped onto an ITO glass support using a dropper, then the TiO_2/C composite/ITO glass electrode was dried in air at room temperature for 3 days.

Raman spectra were obtained with a Raman spectrometer (Accuman (SR-510 Pro), Ocean Optics, American) using a 785 nm laser. The laser was focused on a spot with diameter of 0.2–2 mm at a power of less than 8 mW. Spectra were collected in the range of 200–2400 cm^{-1} at an interval of about 4 cm^{-1}.

2.3 Adsorption experiments

2.3.1 Kinetic experiments. The adsorption tests were carried out in dark batch mode at ambient temperature and atmospheric pressure. Typically, 80 mg of the TiO_2/C composite was added to a 250 ml quartz beaker with 100 ml of MB solution (14 mg l^{-1}) and magnetically stirred at a speed of 250 rpm for 2 h. About 0.7 ml of the solution was taken by a syringe at an interval of 15 min, which was separated from the TiO_2/C composite power by a dipped filter net tube of stainless steel. The concentration of MB was determined by measuring the absorbance at 664 nm (λ_{max} for MB), using a UV-vis spectrophotometer (Lambda 35, PerkinElmer, American).

2.3.2 Equilibrium experiments. In the equilibrium experiment, the same conditions as in the kinetic experiment were employed, except that the adsorption time was 24 h and the MB solution was sampled only at the end of the experiment.

The adsorption amount at equilibrium (q_e), adsorption amount (q_t) and percentage of adsorption removal (photocatalytic degradation) at any time t were calculated as follows:

$$q_e = \frac{(C_0 - C_e)V}{m} \tag{1}$$

$$q_t = \frac{(C_0 - C_t)V}{m} \tag{2}$$

Adsorption removal (photocatalytic degradation) (%)

$$= \frac{(C_0 - C_t)}{C_0} \times 100\% \tag{3}$$

where C_0 (mg l^{-1}), C_e (mg l^{-1}) and C_t (mg l^{-1}) are the MB concentrations initially, at equilibrium time and at time t (min), respectively. V (l) is the volume of the solution, and m (g) is the weight of the TiO_2/C composite.

2.4 Photocatalytic degradation of methylene blue

The photocatalytic performance of the TiO_2/C composite was evaluated in a self-made photocatalytic device by the photodegradation of MB in aqueous solution under the irradiation of ultraviolet (UV) light with a wavelength of 254 nm. A 15 W UV lamp (light intensity of 0.4 W m^{-2}) served as the light source. Typically, 50 mg of TiO_2/C composite was evenly dispersed in a 100 ml MB aqueous solution with an initial concentration of 14 mg l^{-1} in a self-designed quartz reactor. The mixture was magnetically stirred at a speed of 250 rpm in the dark for a certain time to achieve the equilibrium of adsorption/desorption between the TiO_2/C composite and the substrate. Subsequently, the light source was switched on, and the reactor was cooled by circulating water throughout the experiment. Then, aliquots were sampled at the given irradiation time intervals as in the adsorption experiments. Similarly, the photocatalytic activity was also measured by the photodegradation of MB in aqueous solution on the TiO_2/C composite under the irradiation of visible light with a wavelength of more than 420 nm and power of 140 W. The light intensity of the simulated solar spectrum was *ca.* 925 W m^{-2} (as measured with a digital power meter). The concentration of MB was determined by measuring the absorbance at 664 nm (λ_{max} for MB), using a UV-vis spectrophotometer (Lambda 35, PerkinElmer, American). The percentage of photocatalytic degradation is described by eqn (3): $(1 - C_t/C_0) \times 100\%$, where C_0 and C_t are respectively the MB concentrations initially and at time t.

3. Results and discussion

3.1 Textural and structural properties of TiO_2/C composites

The chemical compositions, specific surface areas and pore structural parameters of the TiO_2/C composites are summarized in Table 1. The content of TiO_2 was 61.1%, 65.0%, 65.3% and 67.0% for the TiO_2/C-650, TiO_2/C-700, TiO_2/C-750 and TiO_2/C-800, respectively. Thus, the content of TiO_2 in the TiO_2/C composite was higher than the desired value and increased with the increase in the calcination temperature, indicating that the higher the calcination temperature, the more the carbon oxides formed. Although all TiO_2/C composites showed typical mesopores for the pore size distributions by the BJH method (see Fig. 1(b) below), as seen in Table 1, there were varying degrees of micropores and macropores, and the proportion of mesopores varied from 62% to 73% for these samples.

The above-mentioned carbon oxides could be produced by the reaction between carbon and SO_3 from flour and $Ti(SO_4)_2$ as follows: $xSO_3 + C \rightarrow xSO_2 + CO_x$. Due to the acidity of the $Ti(SO_4)_2$ aqueous solution, by way of dehydration, condensation polymerization, or hydrolysis, flour as a disaccharide can be converted into a polysaccharide, humic acid, or monosaccharide, *etc.* These carbohydrates were carbonized to form

Table 1 Chemical composition, surface area and pore structure of the TiO_2/C composite[a]

Sample	Chemical composition (wt%)		BET area (m^2 g^{-1})	Most probable pore size (nm)	V_{total} (cm^3 g^{-1})	V_{micro} (cm^3 g^{-1})	R_{micro} (%)	V_{meso} (cm^3 g^{-1})	R_{meso} (%)
	TiO_2	C							
TiO_2/C-650	61.1	38.9	138	3.9	0.12	0.021	17.5	0.087	72.5
TiO_2/C-700	65.0	35.0	134	3.9	0.12	0.036	30.0	0.074	61.7
TiO_2/C-750	65.3	34.7	124	3.9	0.12	0.029	24.2	0.089	74.2
TiO_2/C-800	67.0	33.0	117	6.8	0.078	0.027	34.6	0.049	62.8

[a] V_{total}: total pore volume; V_{micro}: micropore volume; V_{meso}: mesopore volume; R_{micro}: $V_{micro}/V_{total} \times 100\%$; R_{meso}: $V_{meso}/V_{total} \times 100\%$.
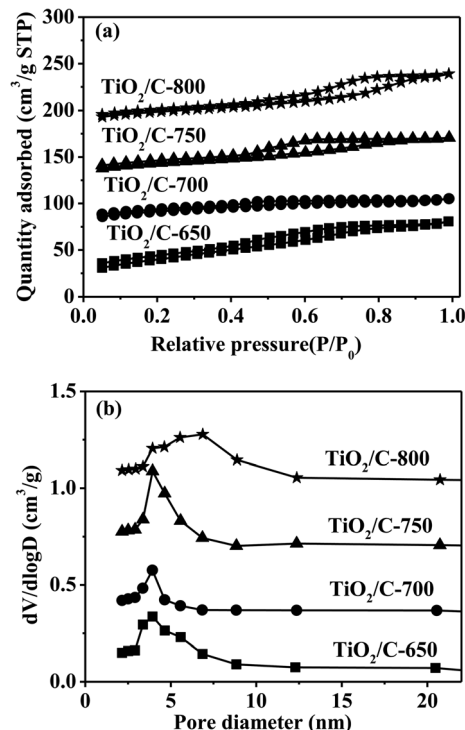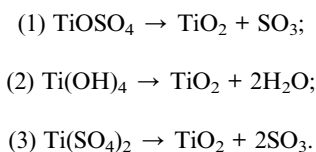
Fig. 1 N$_2$ adsorption/desorption isotherms (a) and pore size distributions (b) of the TiO$_2$/C composites.

carbon at high temperatures. Ti(SO$_4$)$_2$ can be changed into TiOSO$_4$ and Ti(OH)$_4$, which can be dispersed in the polymers formed from flour. These hydrolyzates and unreacted Ti(SO$_4$)$_2$ can be decomposed according to the following reactions at high calcination temperature:

$$(1)\ TiOSO_4 \rightarrow TiO_2 + SO_3;$$

$$(2)\ Ti(OH)_4 \rightarrow TiO_2 + 2H_2O;$$

$$(3)\ Ti(SO_4)_2 \rightarrow TiO_2 + 2SO_3.$$

The TiO$_2$/C composite is produced by all these reactions.

N$_2$ adsorption/desorption isotherms and pore size distributions for the TiO$_2$/C composites calcinated at different temperatures are shown in Fig. 1. The nitrogen adsorption/desorption isotherms for all TiO$_2$/C composites displayed similar hysteresis loops at relative pressures ranging from 0.4 to 0.9, which belong to the type IV isotherms with H2 (b) hysteresis loops, typical of mesopores according to the IUPAC classification.[43] A single peak was observed for the pore size distribution of every sample. The peaks were weak and narrow for the TiO$_2$/C-650 and TiO$_2$/C-700, while strong and broad for the TiO$_2$/C-750 and TiO$_2$/C-800. Table 1 shows that all TiO$_2$/C composites possessed high surface areas (138–117 m^2 g^{-1}), which decreased slowly with the increase of the calcination temperature due to the sintering. The pore diameters and pore volumes derived from the nitrogen adsorption/desorption isotherms of the TiO$_2$/C composites are also listed in Table 1. The most

probable pore sizes and pore volumes (about 3.9 nm and 0.12 cm^3 g^{-1}, respectively) were almost the same for the TiO$_2$/C-650, TiO$_2$/C-700 and TiO$_2$/C-750, while the most probable pore size increased to ca. 6.8 nm, and the pore volume decreased to around 0.078 cm^3 g^{-1} for the TiO$_2$/C-800. This means that more carbon oxides were formed for the TiO$_2$/C-800 obtained at the highest calcination temperature.

XRD patterns of four TiO$_2$/C composites obtained at different calcination temperatures are shown in Fig. 2. No diffraction peaks of graphite crystals were observed in all TiO$_2$/C composites, indicating the presence of highly dispersed or amorphous carbon in the TiO$_2$/C composites. The diffraction peaks at 25.1, 37.9, 48.1, 55.1, 62.7 and 75.7° correspond to (101), (004), (200), (211), (204) and (215) planes of anatase TiO$_2$ (JCPDS 21-1272), respectively. The diffraction peaks at 27.5, 36.1, 39.2, 41.3, 44.1, 56.7, 62.8, 64.1, 69.1 and 69.7° are ascribed to the reflections of the (110), (101), (200), (111), (210), (211), (220), (002), (310), (301) and (112) planes of rutile TiO$_2$ (JCPDS 21-1276), respectively. Only the broad and weak peaks of anatase TiO$_2$ appeared for the TiO$_2$/C-650 composite. The peaks of anatase TiO$_2$ became stronger and the very weak peaks of a little rutile TiO$_2$ appeared at the same time for the TiO$_2$/C-700 composite. Only the peaks of a little anatase TiO$_2$ were present and the narrow and strong peaks of more rutile TiO$_2$ appeared due to the transformation of most of the anatase to rutile for the TiO$_2$/C-750 composite obtained at higher calcination temperature. With the calcination temperature further increased to 800 °C, all anatase TiO$_2$ disappeared and completely transformed into rutile TiO$_2$ for the TiO$_2$/C-800 composite. Therefore, with increasing calcination temperature from 650 to 800 °C for the TiO$_2$/C composite, the anatase TiO$_2$ gradually changed into the rutile TiO$_2$, whose corresponding characteristic peaks also became stronger, indicating the gradual increase of the crystal size. The most intense peaks of anatase TiO$_2$ (101) and rutile TiO$_2$ (110) were used to calculate the crystalline size of TiO$_2$ in the TiO$_2$/C composites by the Scherrer equation.[44] The calculated average crystalline sizes of TiO$_2$ are respectively 8.6, 13.9, 20.2 and 27.0 nm for the TiO$_2$/C-650, TiO$_2$/C-700, TiO$_2$/C-750 and TiO$_2$/C-800.

The morphology and structure of the TiO$_2$/C composites were characterized by SEM, as shown in Fig. 3. It can be seen that all TiO$_2$/C composites were composed of spherical nanoparticles or agglomerates with many pores or gaps among them. The sizes of the pores or gaps were nearly the same for the TiO$_2$/
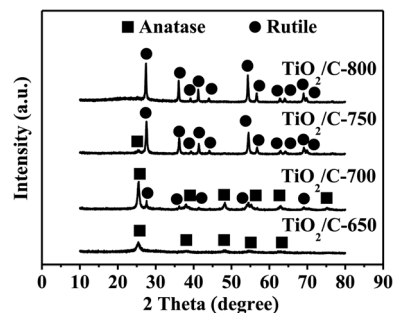

Fig. 2 XRD patterns of the TiO$_2$/C composites.

C-650, TiO$_2$/C-700 and TiO$_2$/C-750, while they became bigger for the TiO$_2$/C-800, in line with the results in pore size distributions. However, the agglomeration of the spherical particles became more and more serious with the increase in the calcination temperature, resulting in the formation of larger particles, in accordance with the XRD results.

To distinguish TiO$_2$ from carbon and estimate its crystal size, TiO$_2$/C-800 as a representative with the best photocatalytic activity (see Fig. 9) was characterized using high-resolution transmission electron microscopy. As shown in Fig. 4, the images suggest that spherical TiO$_2$ nanoparticles or agglomerates were dispersed in the TiO$_2$/C-800. The sizes of these particles were mainly in the range of 22–35 nm, which is consistent with the XRD results.

It was very easy to detect Raman spectroscopy signals for the material's crystallinity and microstructure. The nature of carbon present in the TiO$_2$/C composite was also investigated by Raman spectroscopy since no peaks of carbon existed in the XRD patterns, as shown in Fig. 5. All TiO$_2$/C composites showed two broad and weak peaks at around 1342 and 1590 cm^{-1}, namely the D-band and G-band, except that the G-band peak in the TiO$_2$/C-650 was at about 1560 cm^{-1}. The G-band is assigned to graphitic carbon with sp^2 hybrid while the D-band is ascribed to the defects present in the hexagonal graphitic structure. Compared with pure graphite, some imperfect structures of carbon caused the shift in the maximum wavenumbers for G-band peaks in the TiO$_2$/C composites.[45] The intensity ratios of the G-band and D-band (I_G/I_D) were respectively 0.62, 0.69, 0.77 and 0.87 for the TiO$_2$/C-650, TiO$_2$/C-700, TiO$_2$/C-750 and TiO$_2$/C-800, indicative of the enhanced carbon graphitization as a result of the increased calcination temperature.
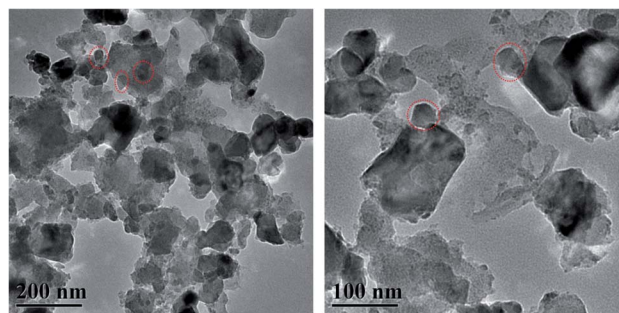

Fig. 4 TEM images of the TiO$_2$/C-800 composite.

3.2 Adsorption kinetics and equilibrium adsorption

To determine the time to reach the equilibrium adsorption, the effect of the contact time on the adsorption of MB onto the TiO$_2$/C composite was studied. The amount of adsorbed MB on the TiO$_2$/C-650, TiO$_2$/C-700, and TiO$_2$/C-750 had a little change after 2 h, while the one on the TiO$_2$/C-800 did after 6 h. Therefore, to ensure that absolute equilibrium was established, 24 h was selected as the equilibrium time to determine the adsorption amount at equilibrium (q_e) for all TiO$_2$/C composites, as shown in Table 2. Both the amount of adsorption and percentage removal of MB increased with the increase in the calcination temperature for all TiO$_2$/C composites. This was consistent with the decrease in the BET surface area and the increase in the crystal size, meaning that the graphitized carbon played a key role and had a significant effect on the adsorption of MB for these TiO$_2$/C composites since the adsorptivity of TiO$_2$ is very poor.[46,47]
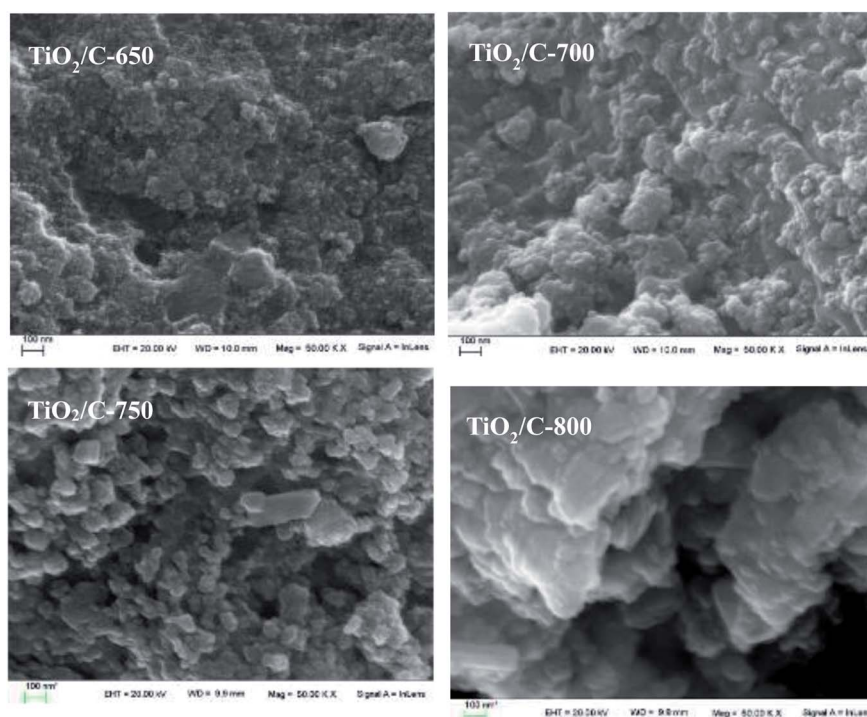

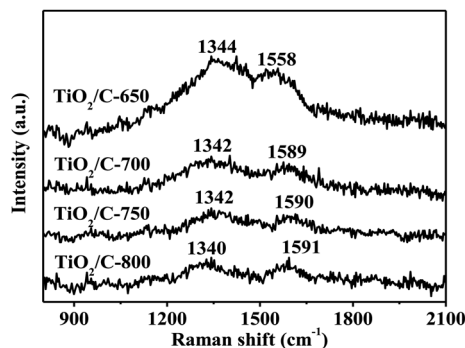Fig. 3 SEM images of the TiO$_2$/C composites.
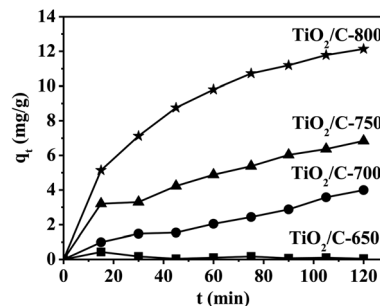
Fig. 5 Raman spectra of the TiO$_2$/C composites.

Fig. 6 Adsorption capacity *versus* contact time for the adsorption of MB on the TiO$_2$/C composite; (m(TiO$_2$/C) = 80 mg, C_0(MB) = 14 mg l^{-1}).

The variations in the amount of adsorbed MB over contact time are shown in Fig. 6. The MB adsorption rate was very small and the concentration of MB had no change in 2 h for the TiO$_2$/C-650. The MB adsorption rates in the initial 15 min were quick and then became slow for the TiO$_2$/C-700, TiO$_2$/C-750 and TiO$_2$/C-800. It was observed that the higher the calcination temperature, the better the TiO$_2$/C composite performance for MB adsorption. Thus, the adsorption capacities of MB on these TiO$_2$/C composites followed the sequence: TiO$_2$/C-650 < TiO$_2$/C-700 < TiO$_2$/C-750 < TiO$_2$/C-800.

Generally, the process of liquid adsorption on a solid includes three steps: (I) film diffusion, (II) intraparticle diffusion or pore diffusion on the surface, (III) sorption onto interior sites.[48] To investigate the mechanism of sorption and potential rate-controlling steps such as mass transport, and chemical reaction processes, four commonly accepted kinetic models were used to fit the present experimental data, which are as follows:[49–54]

Pseudo-first-order model:

$$\ln(q_e - q_t) = \ln q_e - k_1 t \tag{4}$$

Pseudo-second-order model:

$$t/q_t = 1/(k_2 q_e^2) + t/q_e \tag{5}$$

Weber intraparticle diffusion model:

$$q_t = k_{id} t^{0.5} + C \tag{6}$$

Elovich model:

$$q_t = 1/\beta \ln(\alpha\beta) + 1/\beta \ln t \tag{7}$$

Table 2 Adsorption amount and percentage of removal of MB at equilibrium for the TiO$_2$/C composites; (m(TiO$_2$/C) = 80 mg, C_0(MB) = 14 mg l^{-1})

Sample	Adsorption removal (%)	q_e (mg g^{-1})
TiO$_2$/C-650	7.6	1.4
TiO$_2$/C-700	26.4	4.8
TiO$_2$/C-750	55.9	10.2
TiO$_2$/C-800	80.1	14.6

where q_e (mg g^{-1}) and q_t (mg g^{-1}) are the amounts of adsorbed MB at equilibrium and at any time t (min), respectively. k_1 (min^{-1}), k_2 (g mg^{-1} min^{-1}) and k_{id} (mg g^{-1} min$^{-0.5}$) are the rate constants for the pseudo-first-order, pseudo-second-order and intraparticle diffusion models, respectively. α (mg g^{-1} min^{-1}), and β (g mg^{-1}) are the initial adsorption rate and the desorption constant, respectively.

The four models were used to investigate the MB adsorption kinetics only for the TiO$_2$/C-700, TiO$_2$/C-750 and TiO$_2$/C-800, since almost no MB could be adsorbed on the TiO$_2$/C-650. The fitted plots of these adsorption kinetic models are shown in Fig. 7(a–d) and the corresponding model fitting parameters are summarized in Table 3. The validity of each model was checked by the corresponding correlation coefficients (R^2). As seen in Table 3, for the TiO$_2$/C-700, the values of R^2 from the pseudo-first-order, pseudo-second-order, and Elovich models were 0.869, 0.539 and 0.774, respectively. The calculated amount of MB equilibrium adsorption $q_{e, cal}$ (5.4 mg g^{-1}) by the pseudo-first-order model was also closest to that from experiment $q_{e, exp}$ (4.8 mg g^{-1}) for the TiO$_2$/C-700. Similarly, the same rule as for the TiO$_2$/C-700 existed for the TiO$_2$/C-750. However, for the TiO$_2$/C-800, the value of R^2 (0.998) from the pseudo-second-order model was the largest, and there was a minimal difference between $q_{e, cal}$ and $q_{e, exp}$; the fitted plot was also in good agreement with the Elovich model. Therefore, according to the $q_{e, cal}$ and R^2, the pseudo-first-order model was considered as the best-fit in describing the MB adsorption kinetics for the TiO$_2$/C-700 and TiO$_2$/C-750, while the pseudo-second-order model, controlled by chemical adsorption, was the best for the TiO$_2$/C-800.

The Weber intraparticle diffusion model was used to analyze the kinetic data in order to investigate whether intraparticle diffusion was the rate-limiting step in the adsorption process, as shown in Fig. 7(d). A plot of the amount of MB adsorbed (q_t) *versus* $t^{1/2}$ should be linear, and if the line passes through the origin, then intraparticle diffusion is the only rate-controlling step.[53] The plots presented two linear parts, which indicate that the intraparticle diffusion was not the sole rate-controlling step for the TiO$_2$/C-700, TiO$_2$/C-750 and TiO$_2$/C-800.

The results of the transient photocurrent measurements for the TiO$_2$/C composites are shown in Fig. 8. Each TiO$_2$/C composite/ITO glass electrode exhibited a current response to
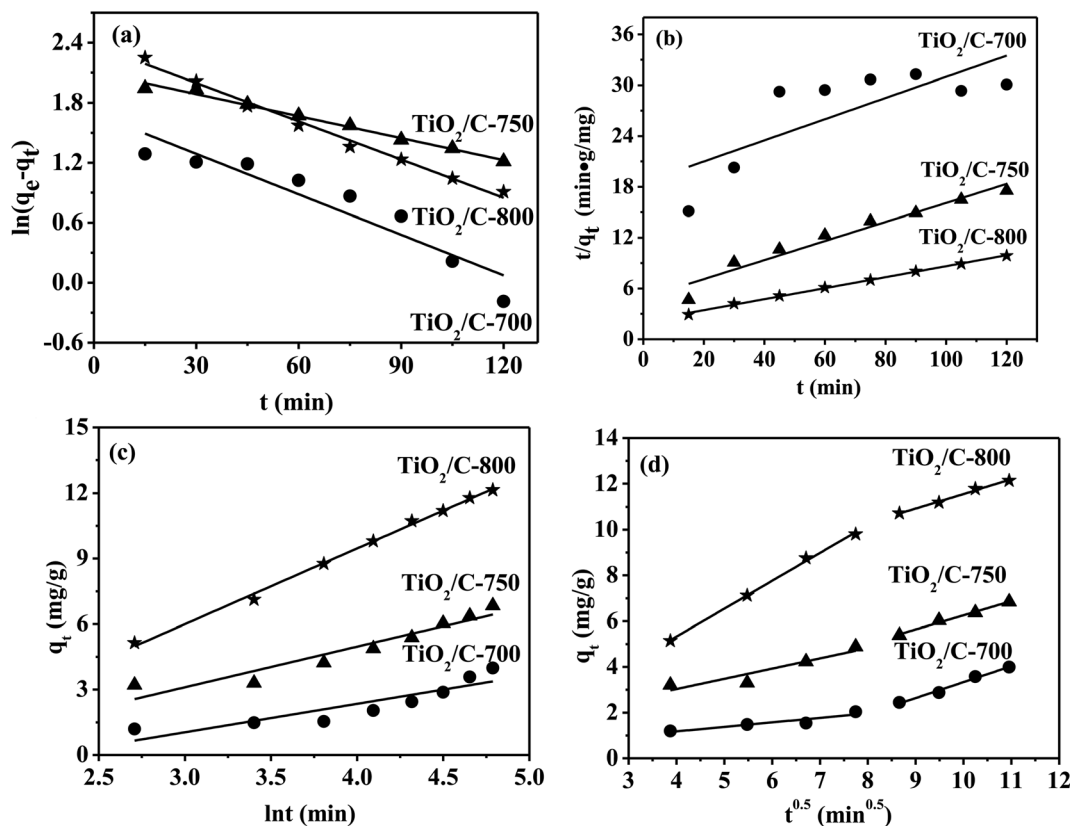
Fig. 7 Fitted plots of (a) pseudo-first-order, (b) pseudo-second-order, (c) Elovich and (d) intraparticle diffusion kinetic models for the adsorption of MB on the TiO_2/C composites. ($m(TiO_2/C) = 80$ mg, $C_0(MB) = 14$ mg l^{-1}).

UV light, and the current rapidly decreased as soon as they were in the dark. The photogenerated current densities remained stable during the irradiation, due to the presence of a contact potential between the TiO_2/C composite particles and ITO glass. This photo-responsive behaviour was completely reversible. It was observed that the photocurrent density was 0.3, 2.5, 8.7 and 11.0 μA cm^{-2} for the TiO_2/C-650, TiO_2/C-700, TiO_2/C-750 and TiO_2/C-800 under the irradiation of UV light, respectively. These results indicated that the separation efficiency of the

photoinduced electrons and holes in the TiO_2/C composites increased with the increase in the calcination temperature, ascribed to the formation of more graphitized carbon.

3.3 Photocatalytic activity

At room temperature and atmospheric pressure, the UV light photocatalytic degradation activity of MB on 50 mg of the TiO_2/C composite is shown in Fig. 8. Compared with the photo-catalytic degradation of MB, the removal of MB adsorption on

Table 3 Parameters for the (a) pseudo-first-order, (b) pseudo-second-order, (c) Elovich and (d) intraparticle diffusion kinetic models for the adsorption of MB on the TiO_2/C composites. ($m(TiO_2/C) = 80$ mg, $C_0(MB) = 14$ mg l^{-1})

| Models	Parameters	TiO_2/C-700	TiO_2/C-750	TiO_2/C-800
Pseudo-first-order equation: $\ln(q_e - q_t) = \ln q_e - k_1 t$	k_1	0.013	0.0073	0.013
	$q_{e, cal}$	5.4	8.2	10.8
	R^2	0.869	0.987	0.989
Pseudo-second-order equation: $t/q_t = 1/(k_2 q_e^2) + t/q_e$	k_2	0.0010	0.0026	0.0020
	$q_{e, cal}$	8.0	8.9	15.4
	R^2	0.539	0.941	0.998
Elovich equation: $q_t = 1/\beta \ln(\alpha\beta) + 1/\beta \ln t$	α	0.14	0.49	0.97
	β	0.77	0.54	0.29
	R^2	0.774	0.895	0.996
The Weber intraparticle diffusion equation: $q_t = k_{id} t^{0.5} + C$	k_{id}	0.20	0.45	1.22
	C	0.39	1.24	0.45
	R^2	0.812	0.812	0.996
Experimental data	$q_{e, exp}$	4.8	10.2	14.6
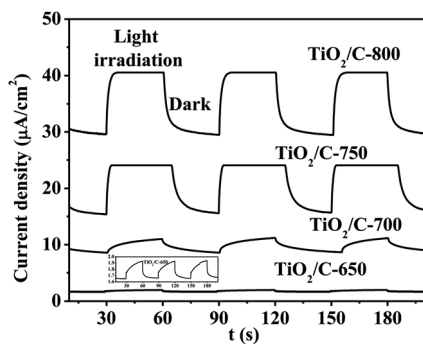
Fig. 8 Transient photocurrent responses of the TiO_2/C composites under UV light irradiation at 0 V vs. SCE; the inset is an enlarged view of the plot for TiO_2/C-650.

characterization, such as specific surface area, crystal phase-type, crystallite size and dispersed surface-active species.[56]

High specific surface area and small crystal size are beneficial for providing more active sites for adsorption and reaction, leading to higher photocatalytic activity.[17] However, the present TiO_2/C composite with higher BET surface area and smaller crystal TiO_2 did not exhibit the better adsorptivity, indicating that the adsorptivity could not be caused only by single physical adsorption and highly dispersed crystal TiO_2. Although the pseudo-first-order model was the best-fitting model in describing the MB adsorption kinetics for the TiO_2/C-700 and TiO_2/C-750, and the pseudo-second-order model for the TiO_2/C-

the TiO_2/C composite was measured under the same conditions except for no light irradiation, as shown in Fig. 9(a). The adsorption equilibrium approximately reached the adsorption in the dark since the concentration of MB remained almost unchanged after 2.5 h. Therefore, in the photocatalytic degradation of MB, 2.5 h was selected for MB adsorption on the TiO_2/ C composites in the dark, and then the mixture was irradiated for 3 h again under a 15 W UV light source, as shown in Fig. 9(b). The concentration of MB did not change with contact time in the absence of the TiO_2/C composite, indicating no self-degradation of MB. The percentages of photocatalytic degradation of MB were 11.0%, 16.4%, 38.1% and 60.5%, while those of adsorption removal of MB are respectively 4.6%, 13.7%, 26.1% and 35.4% for the TiO_2/C-650, TiO_2/C-700, TiO_2/C-750 and TiO_2/C-800, respectively. The difference between the percentage of photocatalytic degradation and that of adsorption removal was both very small (less than 7%) for the TiO_2/C-650 and TiO_2/C-700, indicating the low activity of the photocatalytic degradation of MB. The differences between the percentage of photocatalytic degradation and that of adsorption removal were 12.0% and 25.1% for the TiO_2/C-750 and TiO_2/C-800, respectively, suggesting enhanced activity with the increase in the calcination temperature. The kinetics of MB photodegradation over the TiO_2/C composite was delineated using the pseudo-first-order kinetics model according to the method in the literature.[55] The results are presented in Fig. 9(c). The reaction rate constants for the TiO_2/C-650, TiO_2/C-700, TiO_2/C-750 and TiO_2/C-800 were 6.8×10^{-4}, 5.5×10^{-4}, 1.3×10^{-3} and 3.4×10^{-3} min^{-1}, respectively. The difference in rate constants for the TiO_2/C-650 and TiO_2/C-700 was very small. The rate constants for the TiO_2/C-750 and TiO_2/C-800 were about 2 and 5 times that for the TiO_2/C-650, respectively. Thus, the performance of UV light photocatalytic degradation of MB on the four TiO_2/C composites followed the sequence: TiO_2/C-800 > TiO_2/C-750 > TiO_2/C-700 > TiO_2/C-650.

In the photocatalysis reaction, the performance of the photocatalyst is mainly determined by the following three properties: the adsorption of reactant, the light absorbance, and the transport and separation of photogenerated carriers.[46,56] These properties are greatly influenced by the surface
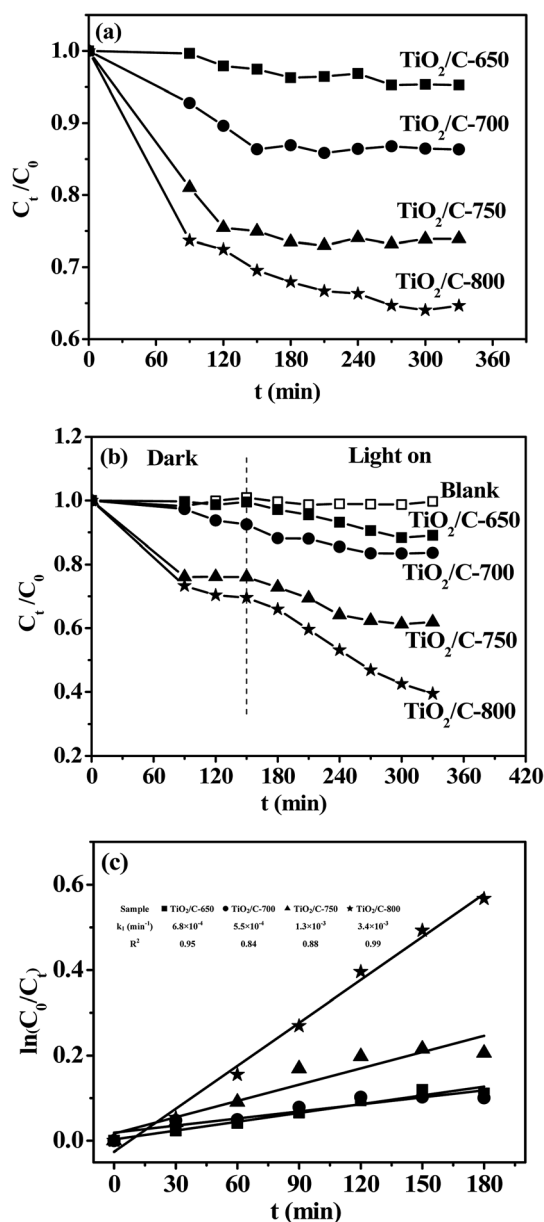

Fig. 9 MB concentration versus contact time for adsorption removal (a), UV light photocatalytic degradation (b) and fitted plots of pseudo first order kinetic model for photocatalytic degradation (c) of MB on the TiO_2/C composites. ($m(TiO_2$/C) = 50 mg, C_0(MB) = 14 mg l^{-1}).

800, the corresponding correlation coefficients (R^2) from the pseudo-second-order model increased with the increase in the calcination temperature for these TiO_2/C composites. This means that the enhanced adsorptivity should be largely attributed to selective chemical adsorption by the π–π stacking between the aromatics of MB and graphitic carbon in the TiO_2/C composite.[45,46]

The formed encapsulation of the carbon layers can suppress the phase transformation and crystal growth of TiO_2 at the calcination temperature of 800 °C.[46] The anatase gradually became rutile in the TiO_2/C composites on increasing the calcination temperature from 650 to 800 °C. This means that less encapsulation of carbon layers existed in the present TiO_2/C composites. The anatase had higher photoactivity due to its faster rate of diffusion and a lower recombination of charge carriers as compared with rutile for TiO_2; furthermore, a rutile component along with anatase can also enhance the photocatalytic activity.[57] However, the TiO_2/C-700 did not exhibit the highest photocatalytic activity of MB degradation despite having a high BET surface area, small crystal size of TiO_2, and high anatase/rutile ratio; interestingly, the entire rutile TiO_2/C-800 exhibited the highest photocatalytic activity. It was inferred that the graphitic carbon may have a significant effect on not only the adsorptivity, but the light absorbance and the efficiency of transport and the separation of photogenerated carriers. The photocurrent results confirmed the higher efficiency of transport and separation of photogenerated carriers for the TiO_2/C composite with more graphitic carbon. We attempted to measure the absorbance of TiO_2 in the TiO_2/C composites by UV-vis diffuse reflectance spectroscopy but no signals could be detected, probably because the excess carbon absorbed most of the light. Thus, the photocatalytic activities of the TiO_2/C composites were also investigated in the visible light range of the spectrum ($\lambda > 420$ nm), as shown in Fig. 10. Compared with the adsorption removal (in Fig. 9), the percentages of photocatalytic degradation did not change, indicative of no visible light photocatalytic activities for the TiO_2/C-650 and TiO_2/C-700. The differences between the percentage of photocatalytic degradation and that of adsorption removal were 5.9% and 10.6% for the TiO_2/C-750 and TiO_2/C-800, respectively. Therefore, both TiO_2/C-750 and TiO_2/C-800 exhibited lower photocatalytic activity under visible light as compared to under UV light. The results indirectly indicate that graphitic carbon promoted the absorbance of visible light by the formation of the Ti–O–C bond, similar to the case of the P25–GR composites.[46]

To explain the role that carbon plays in the TiO_2/C composite, the photocatalytic performances of three TiO_2 crystalline structures (anatase, the mixture of anatase/rutile, and rutile, see the inset of Fig. 11(a)) were investigated for comparison by heating the corresponding TiO_2/C composites at different temperatures in air. However, the phase of TiO_2 obtained by calcination in air was different from that in an inert gas at the same temperature; *e.g.*, the mixture of anatase/rutile existed in TiO_2 obtained by calcination of the TiO_2/C-650 in air at 650 °C (data not given). Therefore, 550, 700 and 800 °C were respectively selected as calcination temperatures to obtain three TiO_2 crystals (anatase, the mixture of anatase/rutile, and rutile),
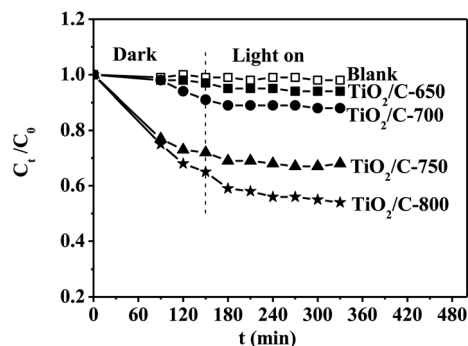

Fig. 10 MB concentration *versus* contact time for the photocatalytic degradation of MB on the TiO_2/C composites under the irradiation of a visible light source with a power of 140 W. ($m(TiO_2/C) = 50$ mg, $C_0(MB) = 14$ mg l^{-1}).

namely TiO_2-550, TiO_2-700 and TiO_2-800. The results of their XRD patterns can be seen in the inset of Fig. 11(a).

At room temperature and atmospheric pressure, the UV light photocatalytic degradation activity of MB on 30 mg of TiO_2 (about equal to the mass of TiO_2 in the composites) is shown in Fig. 11(a). The differences in the percentage of photocatalytic degradation and that of adsorption removal were 22.5%, 39.7% and 6.7% for the TiO_2-550, TiO_2-700 and TiO_2-800, respectively. As seen in Fig. 11(b), the rate constants of the pseudo-first-order reaction for the TiO_2-550, TiO_2-700 and TiO_2-800 were 1.6 ×
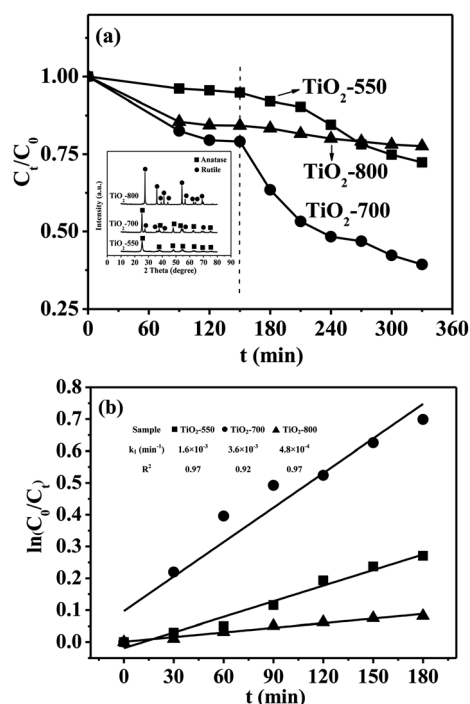

Fig. 11 (a) MB concentration *versus* contact time for UV light photocatalytic degradation. Fitted plots of the pseudo-first-order kinetic model for photocatalytic degradation (b) of MB on the different phases of TiO_2; XRD patterns of these TiO_2 are shown in the inset of (a). ($m(TiO_2) = 30$ mg, $C_0(MB) = 14$ mg l^{-1}).

Table 4 Comparison of the photocatalytic performances for MB degradation on the TiO_2 composites with different carbon materials

Catalyst	Preparation method	Light source	C_0(MB) (mg l^{-1})	Catalyst dose (mg l^{-1})	Rate constant (min^{-1})	Reference
TiO_2 (P25) 3% graphene-like carbon/TiO_2	*In situ* graphitization method	UV (254 nm, 11 W, 0.9 W m^{-2})	10	500	0.1 0.25	26
TiO_2 (P25) 13.5% carbon-doped TiO_2	Solvothermal method	UV (320–390 nm, 70.2 W m^{-2}) + UV (400–780 nm, 452.5 W m^{-2})	25	500	4.60×10^{-3} 8.26×10^{-3}	35
TiO_2 (P25) P25–graphene	Hydrothermal method	UV (365 nm, 100 W, 0.3 W m^{-2})	10	750	4.06×10^{-3} 3.45×10^{-2}	46
TiO_2-550 TiO_2/C-800	Liquid phase reaction combined with calcination	UV (254 nm, 15 W, 0.4 W m^{-2})	14	500	1.6×10^{-3} 3.4×10^{-3}	This work

10^{-3}, 3.6×10^{-3} and 4.8×10^{-4} min^{-1}, respectively. Therefore, the TiO_2-550 and TiO_2-700 had higher photocatalytic activities than the TiO_2/C-650 and TiO_2/C-700 with the same phases of TiO_2, while the TiO_2-800 had lower photocatalytic activity than the TiO_2/C-800. Thus, TiO_2/C-800 had higher photocatalytic activity than pure TiO_2 (anatase or rutile). These results show that carbon nanoparticles could screen the UV light reaching the surface of TiO_2, leading to lower activity.[58] The TiO_2/C-800 had enhanced photocatalytic performance due to the formation of more graphite carbon, which can decrease the recombination of electron/hole pairs and increase the adsorptivity on MB.[59]

To illustrate more clearly what role carbon plays, photocatalytic activities for MB degradation over the TiO_2 composites with different carbon materials are summarized in Table 4. As seen in Table 4, the rate contants of the pseudo-first-order reaction for MB photocatalytic degradation on the same TiO_2 (P25) catalysts were greatly different due to the variety of UV light sources and initial concentrations of MB, *etc.* Doping carbon or the combination with graphite-like carbon can improve the adsorptivity of MB or/and the efficiency of transportation and separation for the photogenerated holes and electrons on the TiO_2, resulting in the significant enhancement of photocatalytic activity; excessive carbon would lead to lower photocatalytic performance. Despite the high carbon content, TiO_2/C-800 with only rutile TiO_2 crystal particles in this work still showed higher photocatalytic activity than pure anatase TiO_2, indicating that the promotion of graphitized carbon was dominant, as compared with its inhibition from the shielding effect.

The graphitic carbon formed has a significant effect on the adsorption of reactant, the light absorbance, and the transport and separation of photogenerated carriers, leading to the enhanced photocatalytic activity for the TiO_2/C composite.

4. Conclusions

(1) The TiO_2/C composite containing approximately 40 wt% carbon was successfully prepared by a method of calcination combined with a one-pot liquid phase reaction. The composite predominantly presented a mesoporous structure with high surface area, highly dispersed TiO_2 and partly graphitized carbon.

(2) No obvious adsorption of MB occurred for the entire anatase TiO_2/C-650; the pseudo-first-order model was the best fit for describing the MB adsorption kinetics for the TiO_2/C-700 and TiO_2/C-750 with the mixture of anatase and rutile, while the pseudo-second-order model, controlled by chemical adsorption, was for the entire rutile TiO_2/C-800.

(3) With the increase in the calcination temperature from 650 to 800 °C for the TiO_2/C composite, the BET surface area decreased, together with the increase in the rutile of TiO_2 and crystal size. However, the TiO_2/C composite with more rutile TiO_2 and graphitic carbon exhibited better adsorption capacity, due to the presence of the graphitic carbon, strongly interacting with MB by offset face-to-face stacking *via* π–π conjugation.

(4) Besides the adsorption of MB, the graphitized carbon can also promote the light absorbance and the efficiency of the transport and separation of photoinduced electrons and holes. Thus, the synergistic effect of adsorption-enrichment and the photocatalytic degradation of MB on the TiO_2/C composite was realized, and the photocatalytic activity of the TiO_2/C composite increased with increasing the calcination temperature from 650 to 800 °C.

(5) Notably, all the intensity ratios of the G-band and D-band (I_G/I_D) in the TiO_2/C composites were less than 1. Thus, with further enhancement of the content of graphitized carbon in the TiO_2/C composite by optimization of the parameters such as calcination temperature, carbon content and other aspects of the preparation procedure, the photocatalytic performance of the TiO_2/C composite is expected to be remarkably improved.

Conflicts of interest

We declare that we do not have any commercial or associative interest that represents a conflict of interest in connection with the work submitted.

Acknowledgements

References

1 M. T. Yagub, T. K. Sen, S. Afroze and H. M. Ang, Dye and its removal from aqueous solution by adsorption: a review, *Adv. Colloid Interface Sci.*, 2014, **209**, 172–184.

2 K. B. Tan, M. Vakili, B. A. Horri, P. E. Poh, A. Z. Abdullah and B. Salamatinia, Adsorption of dyes by nanomaterials: recent developments and adsorption mechanisms, *Sep. Purif. Technol.*, 2015, **150**, 229–242.

3 C. Santhosh, V. Velmurugan, G. Jacob, S. K. Jeong, A. N. Grace and A. Bhatnagar, Role of nanomaterials in water treatment applications: a review, *Chem. Eng. J.*, 2016, **306**, 1116–1137.

4 Z. Cai, Y. Sun, W. Liu, F. Pan, P. Sun and J. Fu, An overview of nanomaterials applied for removing dyes from wastewater, *Environ. Sci. Pollut. Res.*, 2017, **24**(19), 15882–15904.

5 J. Chang, J. Ma, Q. Ma, D. Zhang, N. Qiao, M. Hu, *et al.*, Adsorption of methylene blue onto Fe_3O_4/activated montmorillonite nanocomposite, *Appl. Clay Sci.*, 2016, **119**, 132–140.

6 F. Zhang, X. Chen, F. Wu and Y. Ji, High adsorption capability and selectivity of ZnO nanoparticles for dye removal, *Colloids Surf., A*, 2016, **509**, 474–483.

7 W. Zou, B. Gao, Y. S. Ok and L. Dong, Integrated adsorption and photocatalytic degradation of volatile organic compounds (VOCs) using carbon-based nanocomposites: a critical review, *Chemosphere*, 2019, **218**, 845–859.

8 D. Sud and P. Kaur, Heterogeneous photocatalytic degradation of selected organophosphate pesticides: a review, *Crit. Rev. Environ. Sci. Technol.*, 2012, **42**(22), 2365–2407.

9 K. Nakata and A. Fujishima, TiO_2 photocatalysis: design and applications, *J. Photochem. Photobiol., C*, 2012, **13**(3), 169–189.

10 N. A. Ab Aziz, P. Palaniandy, H. A. Aziz and I. Dahlan, Review of the mechanism and operational factors influencing the degradation process of contaminants in heterogenous photocatalysis, *J. Chem. Res.*, 2016, **40**(11), 704–712.

11 X. Bian and R. Ji, Photocatalytic degradation of methyl blue by tourmaline-coated TiO_2 nanoparticles, *Desalin. Water Treat.*, 2016, **57**(41), 19292–19300.

12 A. Kumar, V. Sharma, S. Kumar, A. Kumar and V. Krishnan, Towards utilization of full solar light spectrum using green plasmonic Au–TiO_x photocatalyst at ambient conditions, *Surf. Interfaces*, 2018, **11**, 98–106.

13 V. Sharma, R. Balaji, A. Kumar, N. Kumari and V. Krishnan, Bioinspired 3 D Surface-Enhanced Raman Spectroscopy Substrates for Surface Plasmon Driven Photoxidation Reactions: Role of Catalyst and Substrate in Controlling the Selectivity of Product Formation, *ChemCatChem*, 2018, **10**(5), 975–979.

14 A. Kumar, K. Kumar and V. Krishnan, Sunlight driven methanol oxidation by anisotropic plasmonic Au nanostructures supported on amorphous titania: influence of morphology on photocatalytic activity, *Mater. Lett.*, 2019, **245**, 45–48.

15 Y. Kuwahara and H. Yamashita, Efficient photocatalytic degradation of organics diluted in water and air using TiO_2 designed with zeolites and mesoporous silica materials, *J. Mater. Chem.*, 2011, **21**(8), 2407–2416.

16 S. A. Lee, K. H. Choo, C. H. Lee, H. I. Lee, T. Hyeon, W. Choi, *et al.*, Use of ultrafiltration membranes for the separation of TiO_2 photocatalysts in drinking water treatment, *Ind. Eng. Chem. Res.*, 2001, **40**(7), 1712–1719.

17 A. Bhattacharyya, S. Kawi and M. B. Ray, Photocatalytic degradation of orange II by TiO_2 catalysts supported on adsorbents, *Catal. Today*, 2004, **98**(3), 431–439.

18 S. Kalikeri, N. Kamath, D. J. Gadgil and V. S. Kodialbail, Visible light-induced photocatalytic degradation of Reactive Blue-19 over highly efficient polyaniline-TiO_2 nanocomposite: a comparative study with solar and UV photocatalysis, *Environ. Sci. Pollut. Res.*, 2018, **25**(4), 3731–3744.

19 P. Benjwal and K. K. Kar, Simultaneous photocatalysis and adsorption based removal of inorganic and organic impurities from water by titania/activated carbon/carbonized epoxy nanocomposite, *J. Environ. Chem. Eng.*, 2015, **3**(3), 2076–2083.

20 W. Li, C. Shang and X. Li, A one-step thermal decomposition method to prepare anatase TiO_2 nanosheets with improved adsorption capacities and enhanced photocatalytic activities, *Appl. Surf. Sci.*, 2015, **357**, 2223–2233.

21 G. Zhang, B. Wang, Z. Sun, S. Zheng and S. Liu, A comparative study of different diatomite-supported TiO_2 composites and their photocatalytic performance for dye degradation, *Desalin. Water Treat.*, 2016, **57**(37), 17512–17522.

22 L. Laysandra, M. W. M. K. Sari, F. E. Soetaredjo, K. Foe, J. N. Putro, A. Kurniawan, *et al.*, Adsorption and photocatalytic performance of bentonite-titanium dioxide composites for methylene blue and rhodamine B decoloration, *Heliyon*, 2017, **3**(12), e00488.

23 J. Shi, Y. Kuwahara, T. An and H. Yamashita, The fabrication of TiO_2 supported on slag-made calcium silicate as low-cost photocatalyst with high adsorption ability for the degradation of dye pollutants in water, *Catal. Today*, 2017, **281**, 21–28.

24 B. Zhang, Q. Wang, J. Zhuang, S. Guan and B. Li, Molten salt assisted in situ synthesis of TiO_2/g-C_3N_4 composites with enhanced visible-light-driven photocatalytic activity and adsorption ability, *J. Photochem. Photobiol., A*, 2018, **362**, 1–13.

25 X. Zhou, S. Zhou, F. Ma and Y. Xu, Synergistic effects and kinetics of rGO-modified TiO_2 nanocomposite on adsorption and photocatalytic degradation of humic acid, *J. Environ. Manage.*, 2019, **235**, 293–302.

26 Y. Wang, R. Shi, J. Lin and Y. Zhu, Significant photocatalytic enhancement in methylene blue degradation of TiO_2

photocatalysts via graphene-like carbon in situ hybridization, *Appl. Catal., B*, 2010, **100**(1–2), 179–183.

27 R. Giovannetti, E. Rommozzi, M. Zannotti and C. A. D'Amato, Recent advances in graphene based TiO₂ nanocomposites (GTiO₂Ns) for photocatalytic degradation of synthetic dyes, *Catalysts*, 2017, **7**(10), 305.

28 Y. Li, S. Zhang, Q. Yu and W. Yin, The effects of activated carbon supports on the structure and properties of TiO₂ nanoparticles prepared by a sol-gel method, *Appl. Surf. Sci.*, 2007, **253**(23), 9254–9258.

29 Z. Lei, Y. Xiao, L. Dang, W. You, G. Hu and J. Zhang, Nickel-catalyzed fabrication of SiO₂, TiO₂/graphitized carbon, and the resultant graphitized carbon with periodically macroporous structure, *Chem. Mater.*, 2007, **19**(3), 477–484.

30 Y. Yao, G. Li, S. Ciston, R. M. Lueptow and K. A. Gray, Photoreactive TiO₂/carbon nanotube composites: synthesis and reactivity, *Environ. Sci. Technol.*, 2008, **42**(13), 4952–4957.

31 Y. Liu, S. Yang, J. Hong and C. Sun, Low-temperature preparation and microwave photocatalytic activity study of TiO₂-mounted activated carbon, *J. Hazard. Mater.*, 2007, **142**(1–2), 208–215.

32 Y. Tao, S. Schwartz, C. Wu and D. W. Mazyck, Development of a TiO₂/AC composite photocatalyst by dry impregnation for the treatment of methanol in humid air streams, *Ind. Eng. Chem. Res.*, 2005, **44**(19), 7366–7372.

33 X. Wang, Z. Hu, Y. Chen, G. Zhao, Y. Liu and Z. Wen, A novel approach towards high-performance composite photocatalyst of TiO₂ deposited on activated carbon, *Appl. Surf. Sci.*, 2009, **255**(7), 3953–3958.

34 F. Dong, H. Wang and Z. Wu, One-step "green" synthetic approach for mesoporous C-doped titanium dioxide with efficient visible light photocatalytic activity, *J. Phys. Chem. C*, 2009, **113**(38), 16717–16723.

35 J. Matos, A. Garcia, L. Zhao and M. M. Titirici, Solvothermal carbon-doped TiO₂ photocatalyst for the enhanced methylene blue degradation under visible light, *Appl. Catal., A*, 2010, **390**(1–2), 175–182.

36 F. Dong, S. Guo, H. Wang, X. Li and Z. Wu, Enhancement of the visible light photocatalytic activity of C-doped TiO₂ nanomaterials prepared by a green synthetic approach, *J. Phys. Chem. C*, 2011, **115**(27), 13285–13292.

37 X. Yan, B. K. Tay and Y. Yang, Dispersing and functionalizing multiwalled carbon nanotubes in TiO₂ sol, *J. Phys. Chem. B*, 2006, **110**(51), 25844–25849.

38 Q. Xiao, J. Zhang, C. Xiao, Z. Si and X. Tan, Solar photocatalytic degradation of methylene blue in carbon-doped TiO₂ nanoparticles suspension, *Sol. Energy*, 2008, **82**(8), 706–713.

39 H. Yu, X. Quan, S. Chen and H. Zhao, TiO₂-multiwalled carbon nanotube heterojunction arrays and their charge separation capability, *J. Phys. Chem. C*, 2007, **111**(35), 12987–12991.

40 C. S. Kuo, Y. H. Tseng, C. H. Huang and Y. Y. Li, Carbon-containing nano-titania prepared by chemical vapor deposition and its visible-light-responsive photocatalytic activity, *J. Mol. Catal. A: Chem.*, 2007, **270**(1–2), 93–100.

41 R. Liu, Y. Ren, Y. Shi, F. Zhang, L. Zhang, B. Tu, *et al.*, Controlled synthesis of ordered mesoporous C-TiO₂ nanocomposites with crystalline titania frameworks from organic-inorganic-amphiphilic coassembly, *Chem. Mater.*, 2008, **20**(3), 1140–1146.

42 Y. Gu, W. Wen and J. Wu, Simple air calcination affords commercial carbon cloth with high areal specific capacitance for symmetrical supercapacitors, *J. Mater. Chem. A*, 2018, **6**(42), 21078–21086.

43 M. Thommes, K. Kaneko, A. V. Neimark, J. P. divier, F. Rodriguez-Reinoso, J. Rouquerol, *et al.*, Physisorption of gases, with special reference to the evaluation of surface area and pore size distribution (IUPAC Technical Report), *Pure Appl. Chem.*, 2015, **87**(9–10), 1051–1069.

44 W. N. Schreiner and R. Jenkins, Profile fitting for quantitative analysis in X-Ray powder diffraction, *Adv. X-Ray Anal.*, 1983, **26**, 141–147.

45 L. Zhang, H. Fu and Y. Zhu, Efficient TiO₂ photocatalysts from surface hybridization of TiO₂ particles with graphite-like carbon, *Adv. Funct. Mater.*, 2008, **18**(15), 2180–2189.

46 H. Zhang, X. Lv, Y. Li, Y. Wang and J. Li, P25-graphene composite as a high performance photocatalyst, *ACS Nano*, 2010, **4**(1), 380–386.

47 C. Hu, F. Chen, T. Lu, C. Lian, S. Zheng, Q. Hu, *et al.*, Water-phase strategy for synthesis of TiO₂-graphene composites with tunable structure for high performance photocatalysts, *Appl. Surf. Sci.*, 2014, **317**, 648–656.

48 X. Peng, D. Huang, T. Odoom-Wubah, D. Fu, J. Huang and Q. Qin, Adsorption of anionic and cationic dyes on ferromagnetic ordered mesoporous carbon from aqueous solution: equilibrium, thermodynamic and kinetics, *J. Colloid Interface Sci.*, 2014, **430**, 272–282.

49 Y. S. Ho and G. Mckay, A comparison of chemisorption kinetic models applied to pollutant removal on various sorbents, *Trans. IChemE*, 1998, **76**(4), 332–340.

50 Y. S. Ho and G. Mckay, Pseudo-second order model for sorption processes, *Process Biochem.*, 1999, **34**(5), 451–465.

51 G. F. Malash and M. I. El-Khaiary, Piecewise linear regression: a statistical method for the analysis of experimental adsorption data by the intraparticle diffusion models, *Chem. Eng. J.*, 2010, **163**(3), 256–263.

52 M. Ghaedi, A. M. Ghaedi, B. Mirtamizdoust, S. Agarwal and V. K. Gupta, Simple and facile sonochemical synthesis of lead oxide nanoparticles loaded activated carbon and its application for methyl orange removal from aqueous phase, *J. Mol. Liq.*, 2016, **213**, 48–57.

53 Z. Ezzeddine, I. Batonneau-Gener, Y. Pouilloux and H. Hamad, Removal of methylene blue by mesoporous CMK-3: kinetics, isotherms and thermodynamics, *J. Mol. Liq.*, 2016, **223**, 763–770.

54 B. Wang, B. Gao and Y. Wan, Comparative study of calcium alginate, ball-milled biochar, and their composites on aqueous methylene blue adsorption, *Environ. Sci. Pollut. Res.*, 2019, **26**(12), 11535–11541.

55 Y. Xu, W. Wen and J. Wu, Titania nanowires functionalized polyester fabrics with enhancedphotocatalytic and antibacterial performances, *J. Hazard. Mater.*, 2018, **343**, 285–297.

56 J. Kou, C. Lu, J. Wang, Y. Chen, Z. Xu and R. S. Varma, Selectivity enhancement in heterogeneous photocatalytic transformations, *Chem. Rev.*, 2017, **117**(3), 1445–1514.

57 J. H. Johnston and A. C. Small, Photoactivity of nano-structured calcium silicate-titanium dioxide composite materials, *J. Mater. Chem.*, 2011, **21**(4), 1240–1245.

58 V. Vaiano, O. Sacco and M. Matarangolo, Photocatalytic degradation of paracetamol under UV irradiation using TiO_2-grahite composites, *Catal. Today*, 2018, **315**, 230–236.

59 D. Awfa, M. Ateia, M. Fujii, M. S. Johnson and C. Yoshimura, Photodegradation of pharmaceuticals and personal care products in water treatment using carbonaceous-TiO_2 composites: a critical review of recent literature, *Water Res.*, 2018, **142**, 26–45.